Plasmonic decay in a metallic grating after femtosecond pulse excitation

Roland Müller and Jens Bethge
Max-Born-Institut, Max-Born-Straße 2a, D-12489 Berlin, Germany
(Received 30 April 2010; published 7 September 2010)

The paper presents a theoretical study on the excitation of surface plasmon polaritons (SPPs) and their decay by reradiation to light. We consider a free-standing metallic transmission grating being illuminated with a TM-polarized light pulse of 10 fs duration at normal incidence. The SPP decay time is assumed to be much larger than the pulse duration. In particular, we analyze the SPP decay after the exciting pulse disappeared. We find periodic amplitude modulation of the declining light field both in close proximity to the grating, where evanescent waves are dominant and in the far-field region, where the light field consists mainly of propagating waves. Using the example of the magnetic field, we demonstrate that the amplitude modulation of the near field exhibits increasing strength with time due to a drop of the evanescent wave density associated with the SPP decay. The far field above and below the grating shows frequency beating with periods corresponding to the reciprocal width of a frequency gap in the transmission spectrum. Strong coupling between SPP modes on the top and bottom interfaces leads to fixed phase relations between the beat notes of the transmitted and reflected light fields. This coupling is confirmed by a periodic change in the Poynting flow direction perpendicular to the interfaces. Finally, we study also the dynamics of the SPP decay by employing Gabor wavelet transforms for the calculated fields far above and below the grating. In this way, we get access to the spectral contents of the light field at different times. This novel spectral-temporal analysis shows a narrowing of the initial pulse spectrum and reveals spectral features not seen in the Fourier spectrum.

DOI: 10.1103/PhysRevB.82.115408 PACS number(s): 73.20.Mf, 71.45.Gm, 24.10.Ht, 79.60.Jv

I. INTRODUCTION

The interaction between light and nanostructured metallic films has drawn attention in the last two or three decades. Among these structures are the optical grating with one-dimensional nanoslits and the two-dimensional nanohole array. Progress made was equally stimulated by the fundamental physical knowledge and its application in diverse areas such as biosensing by use of enhanced Raman scattering,[1] near-field fabrication,[2] and energy transfer across a metal.[3] A key phenomenon of light/metal interaction is the formation of surface plasmon polaritons (SPPs) by collective excitation of the electron density on the surface of a metal by light.[4,5] An SPP comprises an oscillating surface-charge density coupled to an electromagnetic field at the interface of two media with permittivities of opposite sign, for example, a metal and a dielectric. In general, the excitation of SPPs is not possible by simply shining light on a smooth metallic surface because of a momentum mismatch between a photon and the SPP of the same frequency. However, an appropriate periodic structure on the metal surface such as grating slits allows bridging this mismatch, paving the way for the emergence of SPPs. The incident electric field vector has to oscillate perpendicularly to the grating slits for excitation of SPPs on a grating interface, i.e., TM-polarized light is required. The electromagnetic field associated with SPPs is of evanescent character normal to the metal surface, which means that the field decays exponentially with distance from the surface whereas it behaves like a propagating wave (surface mode) in the surface plane.[6] The energy carried by the SPPs is dissipated either nonradiatively by Ohmic losses in the metal or by reradiation into the far field. The latter process is in the focus of this paper.

Generally speaking, SPPs are a particular type of Wood's anomalies occurring in a grating being illuminated by TM-polarized light. These anomalies include two distinct types, namely, a diffraction anomaly and a resonance anomaly. The diffraction anomaly is associated with the observation that at any diffractive order the transition from a propagating to an evanescent wave can be caused by variation of the wavelength or the angle of incidence.[7] The wavelengths at these transitions are the Rayleigh wavelengths λ_R.[8] The resonance anomaly is connected with the excitation of eigenmodes at the grating interface. This case corresponds to the generation of SPPs.[9,10] Both types of anomalies can either occur separately or appear together.[10]

Much attention has been paid to light propagation in periodically nanostructured metallic films in recent years. These studies gave evidence for unexpected transmission properties[11–15] and photonic energy band gaps being responsible for prohibited light propagation within definite frequency intervals.[16–21] These findings have been explained with the existence of SPPs. Extraordinarily high light transmission at certain frequencies in measured spectra was first observed by Ebbesen *et al.*[11] in metallic films perforated with subwavelength hole arrays. Nanostructured metallic gratings were studied experimentally in Refs. 22–27, giving insight into SPP dispersion properties[22,25] and oscillatory light transmission.[23] In theoretical papers, different numerical models are used that relate to light transmission through perforated metallic films.[28–39]

Most of the papers devoted experimentally or theoretically to light propagation in nanostructured metallic films deal with continuous-wave excitation. Only a few are concerned with short-pulse illumination. Some examples for theoretical studies about pulse excitation are presented in Refs. 36–38 and experimental ones in Refs. 23 and 27. In two previous papers, we have theoretically considered the light dynamics in metals perforated with periodic arrays of nanoholes and exciting pulses of 10 fs duration. The first paper[36]

relates to a free-standing symmetric system with air above and below the metallic film whereas the second[37] corresponds to an asymmetric layout with air above and dielectrics with different refractive indices below the film. In both cases, the near field behavior has been investigated exclusively while the transition to the far field, the spectral properties, and the short-time resolution of the spectra have not been considered. In Ref. 38 pulse shaping at transmission through a nanostructured one-dimensional grating is investigated using a finite-difference time-domain (FDTD) model. The authors of Ref. 23 report experimental evidence of periodic patterns superimposed on the transmitted intensity from metallic films with nanoslits after illumination with femtosecond pulses.

The present study deals theoretically with the excitation of SPPs and, in particular, with their decay by reradiation to light in a metallic transmission grating being illuminated with an ultrashort pulse of 10 fs duration at normal incidence. The grating is of symmetric structure surrounded by air. The carrier frequency of the impinging pulse is tuned to maximum transmittance of the grating. This situation corresponds to the excitation of SPPs on both air/metal interfaces. In particular, we analyze the SPP decay after the exciting pulse disappeared. This is done by means of the calculated temporal evolution of the grating light field being closely linked to the SPP decay. The influence of SPPs on the electromagnetic field varies with distance to the grating. Close to the grating, the presence of SPPs manifests itself by *surface* waves E_x, E_z, and H_y moving on the air/metal interfaces. On the other hand, far from the grating *plane* waves E_x and H_y propagating normally to the grating interface indicate an SPP decay due to elastic scattering at the grating slits. The lifetime of the SPPs is assumed to be much larger than the input pulse duration. Thus, after the exciting pulse disappeared, the electromagnetic field is determined by an SPP decay leading to reradiation of photons, i.e., the reverse process of the previous conversion of light to SPPs. This means that pulse excitation allows studying reradiation processes connected to waves of zeroth diffraction order without any interference from external light. However, the short femtosecond pulse illuminating the grating may also excite first-order diffractive propagating waves that superimpose the light waves caused by reradiation of SPPs. Since the different waves belong to different frequency intervals and move in different directions one can clearly distinguish them from each other.

II. THEORETICAL MODEL

The propagation of light through a grating, Fig. 1, is based on Maxwell's equations in combination with an approximate description of the dipole moment on a metal surface following Drude theory.[40] The numerical evaluation is made utilizing an FDTD code, e.g., Refs. 41 and 42. The set of equations used is as follows (SI units)

$$-\frac{\partial H_y}{\partial z} = \varepsilon_0 \frac{\partial E_x}{\partial t} + J_x, \tag{1a}$$

$$\frac{\partial H_y}{\partial x} = \varepsilon_0 \frac{\partial E_z}{\partial t} + J_z, \tag{1b}$$

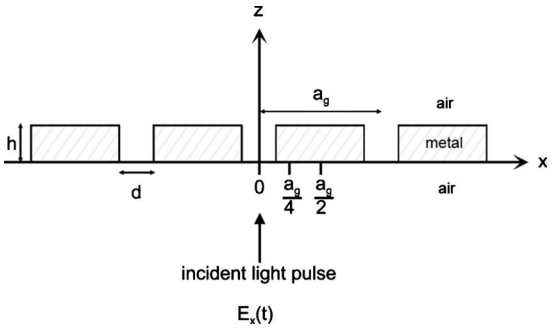

FIG. 1. Schematic illustration of the free-standing transmission grating which the stated theoretical model relates to. Grating parameters: slit width $d=60$ nm, thickness of metal film $h=120$ nm, and lattice period $a_g=750$ nm. The incident 10 fs pulse is TM polarized and illuminates the grating at normal incidence from below.

$$\mu_0 \frac{\partial H_y}{\partial t} = \frac{\partial E_z}{\partial x} - \frac{\partial E_x}{\partial z}, \tag{1c}$$

$$\frac{\partial \vec{J}}{\partial t} + \gamma_D \vec{J} = \varepsilon_0 \omega_D^2 \vec{E}. \tag{1d}$$

Derivatives with respect to y do not appear due to the chosen geometry that is invariant in the y direction. E_x and E_z are the x and z components of the electric field, and H_y is the magnetic field component parallel to the grating slits. The remaining field components disappear, i.e., $E_y=H_x=H_z\equiv 0$. The parameters ε_0 and μ_0 denote the free-space permittivity and magnetic permeability, respectively. The above model is applied to the free-standing grating of Fig. 1, with air above and below the metal film and in the grating slits. Light propagation in these metal-free regions is governed by Eqs. (1a)–(1c) with $J_x=J_z\equiv 0$ whereas description of light propagation in the metal depends on the full set of Eqs. (1a)–(1d). The metal polarization $\vec{P}_m$ is taken into account by J_x and J_z, i.e., the components of a current density vector $\vec{J}(A/cm^2)$. The latter is connected to $\vec{P}_m$ via the time derivative $\vec{J}=\partial \vec{P}_m/\partial t$. Equation (1d) determines the dependence of $\vec{J}$ on $\vec{E}$. According to the Drude model $\vec{J}$ describes the light-induced oscillations of quasifree electrons in the conduction band of the metal. The parameters ω_D and γ_D of Eq. (1d) are related to the relative dielectric function of the metal (gold) $\varepsilon_m=\varepsilon_{m,re}+i\varepsilon_{m,im}$ which is given by the following approximate expression:[20,43]

$$\varepsilon(\omega) = 1 - \frac{\omega_D^2}{\omega^2 + i\gamma_D \omega}. \tag{2}$$

Here ω denotes the angular frequency of light while ω_D and γ_D are chosen to fit empirical data for the real and imaginary parts of ε_m over the (narrow) frequency range of interest around an SPP resonance. The interband contributions[43] to the above dielectric function of gold have been neglected because they are found to be low in the wavelength interval around $\lambda=0.79$ μm being considered in the present paper. It has been estimated from Ref. 43 that the interband transitions contribute less than 2% of $\varepsilon_{m,re}$ and about 10% of $\varepsilon_{m,im}$.

The incident electric field in air is linearly polarized parallel to the x axis and reads as $E_{x,in}(z,t)=A_{in}\cos[\omega_0 t-k_0 z]$, where ω_0 is the free-space carrier frequency and $k_0=\omega_0/c$ is the respective wave number. A_{in} is a Gaussian-shaped function according to $A_{in}=A_0\exp[-2\ln 2\{(t-t_0-z/c)/\tau_0\}^2]$, with A_0 being a real amplitude. τ_0 is the width [full width at half maximum (FWHM)] of the incident pulse intensity time averaged over an optical period, and t_0 denotes a reference time. The corresponding magnetic field is given by $H_{y,in}(z,t)=E_{x,in}(z,t)/Z_0$ with the free-space impedance $Z_0=\sqrt{\mu_0/\varepsilon_0}$.

Light propagation in the grating is treated numerically by applying a two-dimensional FDTD code to Eqs. (1a)–(1d). The space grid is composed of 2×10^2 (x direction) by 2×10^4 (z direction) cells with a space increment of 3.75 nm (maximum number of cells along z is 3×10^4) and the time increment is 5×10^{-3} fs. Periodic boundary conditions are applied to the left and right sides of the unit cell in the x direction whereas second-order Mur conditions terminate the FDTD lattice in the z direction above and below the grating.

Computational results obtained from a numerical model need physical interpretation that should be supported, to the extent possible, by (approximate) analytic relations. For this purpose we will now focus on (i) an approximation by three diffraction modes for the light field above the grating and (ii) a simplified analytic version for the SPP dispersion. Both these methods will help to elucidate findings from our FDTD model.

First, we note that in the case of TM polarization the light field in a one-dimensional grating is fully characterized by its only nonvanishing magnetic component H_y in the current model. We restrict ourselves to the x-z plane above the grating ($z>h$) where the transmitted field H_y reads as

$$H_y(t,x,z-h)=\int_{-\infty}^{+\infty} d\omega e^{-i\omega t}F(\omega)\times\sum_q T_q(\omega)\exp(i[k_{x,q}x+k_{z,q}(z-h)]) \quad (3)$$

with $F(\omega)$ being the Fourier transform of the envelope of the incident Gaussian field. The sum over q corresponds to Rayleigh's expansion, with $T_q(\omega)$ being a complex transmission amplitude. Further, $k_{x,q}$ and $k_{z,q}$ are the components of the wave vector in the x-z plane given by

$$k_{x,q}=qG_x, \quad (4a)$$

$$k_{z,q}=\sqrt{k^2-k_{x,q}^2}, \quad (4b)$$

where $G_x=2\pi/a_g$ is the reciprocal lattice vector in the x direction and $q=0,\pm 1,\ldots$ denotes the diffraction order of grating modes, and $k=\omega/c$ is the free-space wave number. Taking only into account the first three terms of the Rayleigh series ($q=0,\pm 1$), Eq. (3) reduces to the following expression

$$H_y(t,x,z-h)\approx\int_{-\infty}^{+\infty} d\omega e^{-i\omega t}F(\omega)\{T_0\exp[ik(z-h)]+2T_1\cos(G_x x)\exp[i\sqrt{k^2-G_x^2}(z-h)]\} \quad (5)$$

assuming, in addition, consistent expansion coefficients $T_{-1}=T_{+1}=T_1$ for $q=\pm 1$. Corresponding expansions for the electric fields $E_x(t,x,z-h)$ and $E_z(t,x,z-h)$ are obtained by virtue of Eqs. (1a) and (1b), respectively, with $J_x=J_z=0$ in combination with Eq. (5).

The expression in square brackets on the right-hand side of Eq. (5) describes diffractive grating modes belonging to frequency ω and their dependence on the spatial coordinates z and x. For convenience, we briefly summarize the types of diffractive modes excited by TM-polarized light at normal incidence. Referring to the above three-mode approximation one obtains: (i) propagating modes at $q=0$ (specular transmission). The wave vector points in the z direction yielding $k_{x,0}=0$ and $k_{z,0}=k=\omega/c$. (ii) Propagating modes at $q=\pm 1$ and $|k|>G_x$. The wave vector is inclined in respect to the z direction resulting in $k_{x,\pm 1}=\pm G_x$ and $k_{z,+1}=k_{z,-1}=\sqrt{k^2-G_x^2}$. (iii) Evanescent modes at $q=\pm 1$ and $|k|<G_x$. The wave vector points in the x direction with $k_{x,\pm 1}=\pm G_x$ and $k_{z,+1}=k_{z,-1}=i\sqrt{G_x^2-k^2}$.

Generation and decay of SPPs on grating interfaces are intimately connected to the occurrence of appropriate diffraction modes that provide the necessary momentum matching condition for SPP coupling. This can easily be seen, for example, from an approximate SPP dispersion relation for a planar metal/air interface under the assumption that the width of the slits is much smaller than the light wavelength.[4,44] This dispersion relation is then given by

$$k_{SP,x}^{re}=\frac{\omega}{c\sqrt{1+1/\varepsilon_{m,re}}}. \quad (6)$$

Here $k_{SP,x}^{re}$ denotes the real part of the SPP momentum directed along x, parallel to the interface, and ω is the free-space optical frequency. Note that the influence of the slits on the SPP dispersion relation has been ignored in Eq. (6).

First-order SPPs are excited if the condition $k_{SP,x}^{re}=\pm G_x$ is met,[4,45] e.g., by evanescent waves of diffraction order $q=\pm 1$. Actually, an SPP mode can be considered a *leaky* surface mode, given that the SPP momentum is a complex number with $k_{SP,x}^{im}\propto\varepsilon_{m,im}$. The situation is reminiscent of a slightly damped mechanical oscillator that is driven by a force periodically varying with the real eigenfrequency of the oscillator.[9]

The frequency $\omega=\omega_{SP}$ of a first-order SPP can be estimated from Eq. (6) and is approximately given by $\omega_{SP}\approx\omega_R(1+1/2\varepsilon_{m,re})$ making use of the fact that $\varepsilon_{m,re}$ is a large negative number for noble metals in the near infrared part of the spectrum. Since a smooth metal surface is considered ω_{SP} is sometimes referred to as the flat-metal SPP resonance.

The quantity $\omega_R=2\pi c/a_g$ denotes the first-order Rayleigh frequency, i.e., the frequency at which the first diffraction order becomes evanescent according to the grating equation

for normal incidence. Since $|1/2\varepsilon_{m,re}| \ll 1$, the spectral position of ω_{SP} is shifted slightly toward lower frequencies with respect to ω_R. Both, the spectral position of ω_{SP} and its distance to ω_R are quantitatively confirmed by numerically calculated transmission curves, which are based on the above model, Eqs. (1a)–(1d). The reverse process of reradiation arises from the scattering of SPPs at the slits, which results in zeroth-order modes of frequency ω_{SP} propagating normally to the interface.[19]

If one takes into account the grating slits in terms of their dispersive properties, given a periodic modulation of ε_m along x, the simple relation Eq. (6) has to be replaced by a more complex dispersion function, see, for example, Ref. 30. In the present case of normal incidence the input pulse may excite two counterpropagating SPP modes on each of the two air/metal interfaces, on the upper and lower side of the grating. The two SPP modes interfere, giving rise to standing waves. This mode coupling creates a frequency (energy) gap of inhibited light propagation in the dispersion curve.[35] Moreover, coupling between the SPP waves on the top and bottom surfaces may occur due to energy transfer through the grating slits. A frequency gap of very low transmittance with a minimum at ω_{SP} is observed in the grating transmission spectrum (details are given in chapter III.B.).

In this context, we mention that the role of SPPs in the light transmission of metallic gratings has been a subject of debate in recent years.[34] It is now widely accepted that the far-field grating transmission shows a minimum at ω_{SP}, in contrast to the original expectation of a transmission peak.

We close this chapter by specifying the parameter values used for numerical calculations. The geometrical parameters of the grating are as follows: thickness $h=120$ nm, spatial lattice period $a_g=750$ nm, and slit width $d=60$ nm. The exciting pulse is a transform limited Gaussian pulse of 10 fs duration (FWHM of pulse intensity) with a carrier frequency of $\nu_0=0.38$ fs^{-1} ($\lambda_0=0.79$ μm) corresponding to the maximum transmittance of the grating. The real and imaginary parts of the permittivity for the metal (gold) in a narrow range around ν_0 are taken from[46] and read as $\varepsilon_{m,re} \approx -23.3$, $\varepsilon_{m,im} \approx 1.5$. By virtue of Eq. (2) one then obtains $\omega_D \approx 11.7$ fs^{-1} and $\gamma_D \approx 0.15$ fs^{-1}.

III. ELECTRIC FIELDS AND OPTICAL SPECTRA AT VARIOUS DISTANCES FROM THE GRATING

A. Introductory remark

In the following, numerical results are presented that are based on the full set of Eqs. (1a)–(1d). The obtained results are explained using a three-mode approach for the light fields and taking into account properties of the SPPs. It is well known that the field characteristics change strongly with distance from the grating. Treating the simpler case first, subchapter III.B. is devoted to field behavior at distances from the grating larger than the carrier wavelength (intermediate from near-to-far-field region) within a range from 1.9 to 26 μm. Subchapter III.C. refers to the immediate neighborhood of a grating surface (near-field region).

B. Distance from the grating larger than the wavelength

First we want to see how the numerical model used describes the influence of SPPs on the light field. As an example, the *red* curves in the bottom parts of Figs. 2(a) and 2(b) show (a) transmitted and (b) reflected electric fields E_x vs time, which are taken at 3.75 μm above and 3.75 μm below the grating, respectively. The carrier wavelength of the field is $\lambda_0=0.79$ μm being close to the peak transmittance. In both cases, the transverse coordinate is $x=a_g/2$, denoting the horizontal position between two adjacent grating slits.

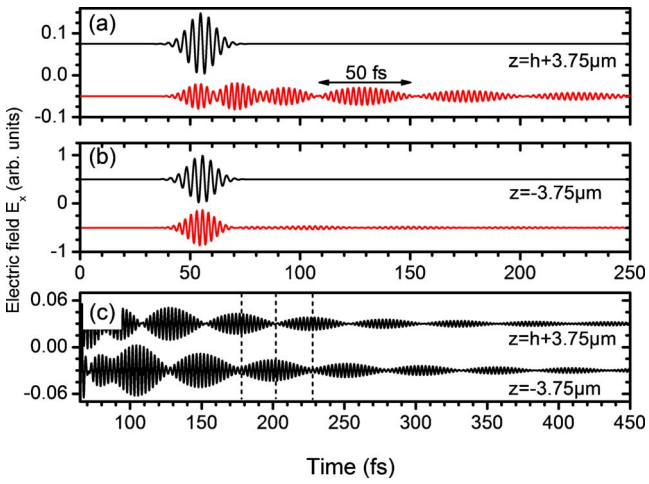

FIG. 2. (Color online) Illustration to explain the effect of SPPs on field dynamics. (a) Transmitted x component of the electric fields E_x vs time beyond the grating at carrier wavelength $\lambda_0=0.79$ μm, red curve (bottom), and $\lambda_0=1.10$ μm, black curve (top). Both curves refer to $z=h+3.75$ μm. (b) The same as (a) but the x component of the reflected electric fields E_x below the grating at $z=-3.75$ μm. (c) Larger view of the beat notes at the trailing edges of the red-colored fields shown in the bottom parts of (a) and (b), respectively, after the input pulse has already decayed, i.e., later than about 70 fs.

The trailing edges of the red curves show damped frequency beats with a period of about 50 fs, which we assume to be due to the light reradiated by SPPs after the incident pulse disappeared. For comparison, the black curves in the top parts of Fig. 2 indicate the transmitted (a) and the reflected (b) field of a 10 fs Gaussian pulse, yet with a carrier wavelength of $\lambda_0=1.10$ μm being significantly outside the peak transmittance. We mention that the two Drude parameters ω_D and γ_D employed in the case of $\lambda_0=1.10$ μm differ only slightly from those for $\lambda_0=0.79$ μm. The two black curves of Figs. 2(a) and 2(b) show no beating characteristics. From this we conclude that frequency beating arises under the condition that the incident light wavelength be sufficiently close to the peak transmittance wavelength.

Moreover, a closer look shows that the antinodes of the beat note above the grating coincide with the nodes of the beat note below the grating and vice versa. Figure 2(c) demonstrates this relationship between the trailing edges in more detail for a prolonged period of time. This behavior of the fields above and below the grating is indicative of a remarkable coupling between the SPPs on the top and bottom surface via the grating slits. We want to emphasize that the beat oscillations of Fig. 2(c) are mainly shaped by propagating waves ($q=0$) since evanescent waves are well negligible at distances of 3.75 μm from the grating. Assuming that the $q=0$ waves are generated by scattering of SPPs in the vicin-

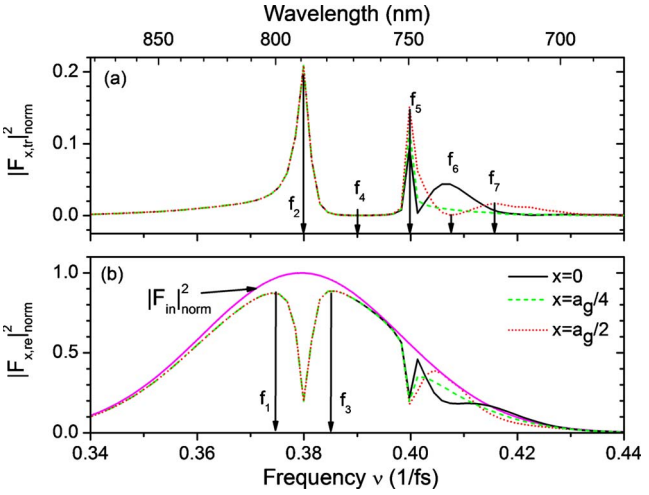

FIG. 3. (Color online) Normalized spectral densities of electric fields vs frequency, above and below the grating, taken at various transverse locations x. The wavelength scale on top has been added for convenience. (a) Spectral density of the transmitted E_x field, 3.75 μm above the grating. (b) Spectral density of the reflected E_x field, 3.75 μm below the grating, and spectral density of the incident pulse.

ity of the two interfaces, after the input pulse died out, one may expect beat notes like that of Fig. 2(c) also in the near field of the grating. However, a pronounced superposition with evanescent waves ($q=\pm 1$) will appear in the near field, see chapter III.C.

In the following, we present calculated optical spectra of the transmitted and reflected E_x fields beyond and below the grating, respectively. The spectra of the E_x fields are described by their spectral densities $|F_x|^2$ vs frequency ν, which are given by the squared absolute values of the Fourier transforms of the E_x fields, that is, $|F_x(\nu)|^2=|\int_{-\infty}^{+\infty}E_x(t)\exp(-i2\pi\nu t)dt|^2$.[47] Figure 3 shows spectral densities, namely, (a) $|F_{x,tr}|^2_{norm}$ of the transmitted E_x field above the grating at $z=h+3.75$ μm for three different transverse positions x, see below, and (b) $|F_{x,re}|^2_{norm}$ of the reflected E_x field below the grating at $z=-3.75$ μm and at the same transverse locations as in (a). Moreover, (b) includes the spectral density $|F_{in}|^2_{norm}$ of the incident Gaussian pulse field. Black (solid), green (dashed), and red (dotted) curves of Figs. 3(a) and 3(b) refer to $x=0$ (center of a grating slit), $x=a_g/4$, and $x=a_g/2$, respectively. All the spectral densities are related to the peak value of the incident spectral density (subscript "norm"). Please, note that the red curves of Figs. 3(a) and 3(b) represent the spectra of the red E_x curves in the bottom parts of Figs. 2(a) and 2(b), respectively.

The spectrum $|F_{x,tr}|^2_{norm}$ of the transmitted field displayed in Fig. 3(a) indicates a frequency interval (gap) of very low transmission, which extends from $f_2\approx 0.38$ fs^{-1} to about $f_5\approx 0.40$ fs^{-1}. The frequency $f_5\equiv f_R=c/a_g$ denotes the Rayleigh frequency. The gap width $\Delta\nu\approx f_5-f_2\approx 0.02$ fs^{-1} correlates with a beat period of nearly 50 fs, as is observed on the transmitted and reflected fields, see Fig. 2. The center of the frequency gap is at $f_4\equiv f_{SP}\approx 0.39$ fs^{-1}, which agrees with the first-order flat-metal SPP resonance, see Eq. (6). Corresponding to an energy shift of 41 meV with respect to f_4, Fig. 3(a) shows that the transmittance peak frequency f_2 is red shifted by about 20 nm, which agrees quite well with measurements.[25] The line shape around f_2 is slightly asymmetrical, indicating a relatively steep increase at the high-frequency side and a slow decrease at the low-frequency side. This behavior agrees qualitatively with transmission spectra deduced from the Fano-type model.[48,49] While the low-frequency edge of the gap at f_2 provides evidence for the occurrence of SPPs, the high-frequency edge appears due to Wood's anomaly.[35] The linewidths around f_2 and f_5 are much narrower than the gap width. This may explain the occurrence of significant beat patterns seen in Fig. 2(c).

For frequencies below f_5 of Fig. 3(a), the three power spectra agree completely, except for a small interval close to f_5. The differences between the peak heights of the three curves seen at f_5 indicate that evanescent waves ($q=\pm 1$) of noticeable amplitude may survive in the immediate vicinity of f_5. However, with a further increase of the distance from the grating, the differences of the peak heights level out. Above f_5, both zero order and first order propagating waves are excited, which gives rise to interference effects dependent on the spatial position (z,x). $|F_{x,tr}|^2_{norm}$ and $|F_{x,re}|^2_{norm}$ behave complementarily over the entire frequency interval, which is evident, for example, from the observation that minima of $|F_{x,re}|^2_{norm}$ coincide with peaks of $|F_{x,tr}|^2_{norm}$ at f_2 and f_5. In contrast, in the interval between these frequencies, low values of $|F_{x,tr}|^2_{norm}$ correlate with high values of $|F_{x,re}|^2_{norm}$.

Since the transmission of light is about 20% for the peak at $f_2=0.38/\text{fs}$, see Fig. 3(a), and the width of the slits is about 8% of the lattice period, we observe a transmission enhancement of approximately 2.5 due to the coupling of light with SPPs. For comparison, the transmission enhancement measured by Ebbesen *et al.*[11] for a hole array was more than 2. Schröter and Heitmann[13] obtained an enhancement factor of roughly 3 from their theoretical grating model.

Summarizing the important features of Figs. 2 and 3, we first note that light transmission through the subwavelength slits of the grating is determined by strong SPP interaction which manifests itself (i) by a frequency gap in the transmission spectrum and (ii) by the temporal behavior of the transmitted field which shows regular beat patterns of a considerable amplitude after the incident pulse disappeared. On the other hand, the effect of SPPs on light reflection is essentially limited to a small-amplitude beat note, whose contribution to the Fourier transform spectrum of the reflected field, therefore, is low. In chapter IV we present detailed insight into the time-dependent spectral properties.

We proceed with the time dependence of the electric fields at several distances above the grating. Again, the carrier wavelength is set to $\lambda_0=0.79$ μm. Figure 4 indicates E_x as a function of time at (a) $z=h+1.875$ μm, (b) $z=h+3.75$ μm, and (c) $z=h+11.25$ μm, where we focus on three transverse positions $x=0$, $x=a_g/4$, and $x=a_g/2$. Figure 4 also displays the electric z component E_z, at $x=a_g/4$. We first note that E_x and E_z of Fig. 4 differ significantly in their temporal characteristics: the E_x fields appear as periodically modulated wave patterns, whereas the E_z fields exhibit nonperiodic monotonic envelope profiles over time. Furthermore, we observe that the onset t_z of E_z oscillations is delayed relative to the arrival

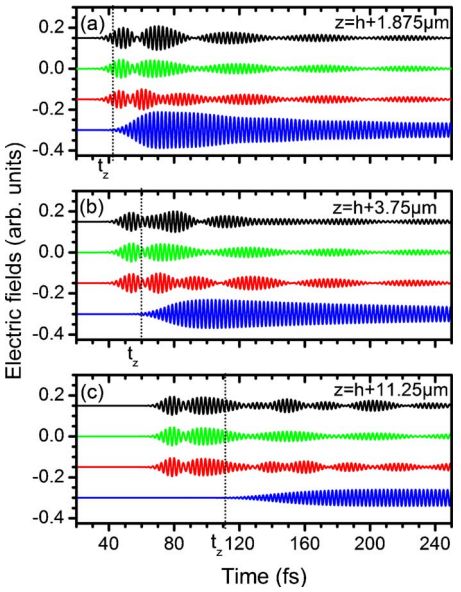

FIG. 4. (Color online) Electric fields E_x and E_z vs time at different distances from the grating: (a) 1.875 μm, (b) 3.75 μm, and (c) 11.25 μm above the grating. Within each subfigure, the three topmost curves describe the x component of the electric field E_x at different transverse positions x, namely, from top to bottom $x=0$ (black curves), $x=a_g/4$ (green), $x=a_g/2$ (red). The bottom most curve displays the z component E_z at $x=a_g/4$ (blue). The time t_z indicates the onset of E_z oscillations.

time of the input pulse and is shifted to later times when z increases.

A more detailed examination of Figs. 4(a) and 4(c) reveals that the green ($x=a_g/4$) wave patterns of E_x look identical at all three distances z provided a shift in time due to the retardation effect is ignored. This is indicative of zero-order waves ($q=0$) propagating in the z direction. The black ($x=0$) and red ($x=a_g/2$) patterns also consist of $q=0$ waves which are, however, partially superimposed by first-order propagating waves ($q=\pm 1$, $\nu>f_5$) and evanescent waves ($q=\pm 1$, $\nu<f_5$). The contribution of the latter to the light field is low at distances from the grating of about twice the wavelength and beyond. However, first-order propagating waves significantly disturb the periodic oscillations of the $q=0$ wave patterns. This can be most clearly observed in Fig. 4(c), at times later than the dotted vertical line at $t \geq t_z$. For $t<t_z$ black and red curves synchronize almost completely with the green ones. This result confirms an expected coincidence of the arrival of diffracted propagating waves at distance z from the grating and the emergence of the E_z field from zero level at time t_z. Disturbances of wave patterns are also observed in Figs. 4(a) and 4(b). Because of partial overlap with the input field, they are less striking when compared to Fig. 4(c).

Figure 4 deals solely with the electric components of the light field. To complete the picture, Fig. 5 describes the time evolution of both, electric *and* magnetic components, taken at a distance from the grating as large as $z=h+26.25$ μm. From top to bottom, the electric fields E_x at $x=0$, $x=a_g/4$, and $x=a_g/2$ are shown. Below E_z at $x=a_g/4$ three more curves belonging to magnetic fields Z_0H_y are plotted for the

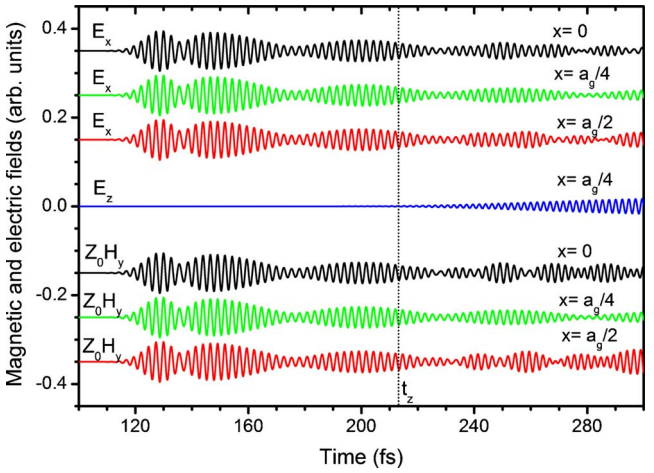

FIG. 5. (Color online) Electric and magnetic fields vs time about 26 μm above the grating at different transverse locations, as indicated on the right-hand side of the plot. At times earlier than indicated by the dotted vertical line, i.e., for $t<t_z$, fields E_x and H_y consist of waves from zeroth-order transmission and oscillate synchronously at the three local positions x. At later times, the phases of the fields no longer agree due to superposition of diffracted (first order) waves.

same transverse positions as the E_x. We observe that all the curves of fields E_x and Z_0H_y completely coincide in the time interval $t<t_z$, before distortions cause nonregular oscillations. This suggests that interfering plane waves propagating in the z direction constitute a wave of slowly modulated amplitude, which is existing in a time interval earlier than indicated by the dotted vertical line. In the far field limit, as z approaches infinity, the time interval $t<t_z$ becomes larger and larger.

One expects that at times earlier than t_z the transmitted energy density flow, is given by the normal component of the Poynting vector, $S_z \equiv E_x H_y$, since energy transport parallel to the grating surface disappears. Figure 6 shows the far-field Poynting flow $\bar{S}_{z,norm}$, where the overbar indicates time aver-

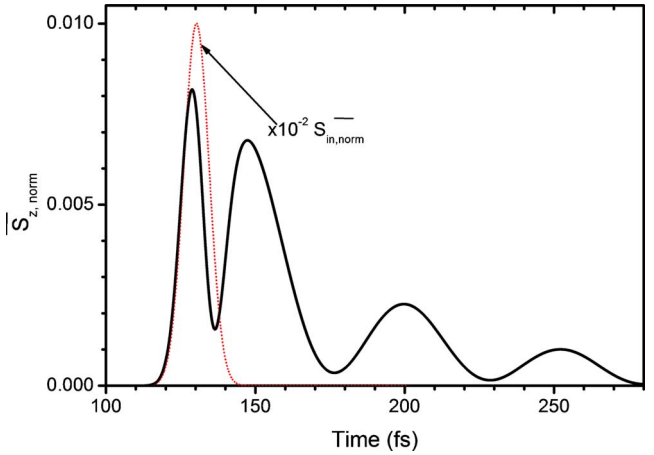

FIG. 6. (Color online) Far-field Poynting flow (time-averaged over an optical cycle) in the z direction vs time. The curve refers to fields E_x and H_y at $x=a_g/4$ of Fig. 5 and is related to the peak value of the incident Poynting flow (red dotted line).

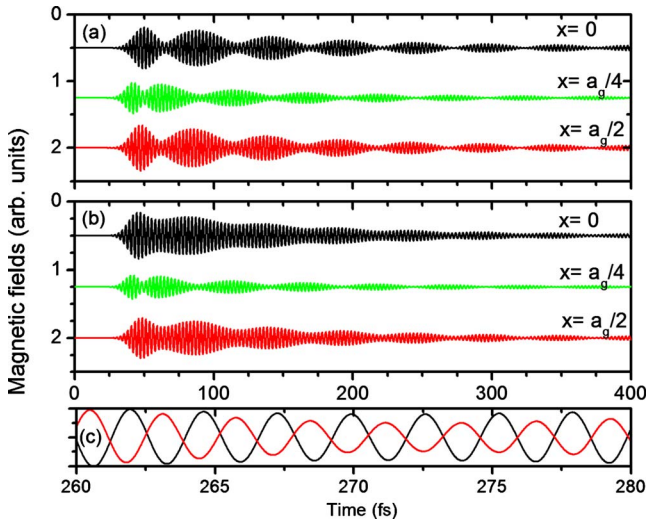

FIG. 7. (Color online) Magnetic near field H_y vs time, (a) 300 nm, (b) 8 nm above the top surface of the grating, and (c) enlarged details of field H_y at the transverse locations $x=0$ and $x=a_g/2$ taken from (b). Note that the green curves of (a) and (b), corresponding to $x=a_g/4$ have been enlarged by a factor of 5.

aging of S_z. The subscript norm means that the Poynting flow is related to the peak value of the input flow.

We end up this chapter with a short reference to two experimental papers dealing with SPP dynamics in nanoslit metallic gratings. The first paper[27] reports femtosecond pump-probe measurements of a perforated gold film deposited on a quartz substrate. After excitation of SPPs with a 100 fs pulse at the two edges of the SPP band gap the authors observed that SPP polarization survives up to nearly 2 ps near the upper energy edge but decays much faster in the case of the other edge. The second paper[23] relates to experiments demonstrating damped periodic modulation of the transmitted light field from a metallic grating deposited on a sapphire substrate. The grating was excited with a 10 fs pulse of carrier wavelength $\lambda_0=800$ nm at oblique incidence ($\vartheta\approx 8°$). The modulation characteristics of the transmitted light after the exciting pulse died out looks similar to the beat note of the calculated red curve in Fig. 2(a).

C. Distance from the grating much smaller than the wavelength

In this chapter we want to examine the temporal field evolution at distances as short as 300 and 8 nm from the top surface of the grating. Figure 7 relates to the behavior of the magnetic field H_y vs time at (a) $z=h+0.300$ μm and (b) $z=h+0.008$ μm. As in previous figures, H_y is calculated for the following transverse locations: $x=0$, $x=a_g/4$, and $x=a_g/2$. Corresponding plots for the electric field intensities $|E_x|^2$ at these locations are given below.

The fields displayed in Figs. 7(a) and 7(b) show periodic amplitude modulations of almost the same modulation period as the beating oscillations seen far above the grating, compare Fig. 2(a). However, this time both the electric and magnetic fields are dominated by evanescent waves, in contrast to the case of larger distances discussed before, where the light field consists mainly of zeroth-order propagating waves.

The evanescent waves in the near field can move in both the positive and negative transverse direction $\pm x$ while their amplitudes decrease exponentially along the z direction. The interference of counterpropagating evanescent waves leads to wave patterns depending on the transverse coordinate, in contrast to propagating zeroth-order waves being independent of x.

The essentially evanescent character of the near field which manifests itself through its particular dependence on x can be seen by means of Eq. (5) assuming that the three-mode model introduced in chapter 2 is still a good approximation in close proximity to a grating surface. The second term in the squared brackets of Eq. (5) describes evanescent waves, if $(2\pi\nu/c)^2-G_x^2<0$, which requires $q=\pm 1$ and $\nu<f_5$. In addition, we find a phase difference by π between evanescent fields at $x=0$ and $x=a_g/2$ which is confirmed in Fig. 7(c), displaying an enlarged portion of the black and red curves of Fig. 7(b). Contributions of zeroth-order waves to both evanescent fields are negligible. However, the zeroth-order waves become visible at locations on the x axis, where a node of interfering evanescent waves appear, that is, at $x=a_g/4$ and at $x=3a_g/4$. The green H_y curve of Fig. 7(b) corresponds to a $q=0$ mode at $x=a_g/4$ showing a very low amplitude in comparison to the evanescent waves.

We observe that the black, green, and red curves of Fig. 7(b) differ from each other by the strength of their amplitude modulation which is usually defined by the modulation index m, that is, the peak-to-valley excursion of the field amplitude divided by the peak height. A closer look reveals that m approaches unity along the green curve, Fig. 7(b). In contrast, the black and red graphs of this figure reveal smaller values of (i.e., $m<<1$), especially at early times. From this we conclude that a high portion of evanescent waves corresponds to a low strength of amplitude modulation, that is, low m. On the other hand, the SPP decay progresses with increasing time. Since this process is connected with the annihilation of evanescent waves and the creation of zeroth-order propagating waves, we expect that m increases with time. In fact, both the black and red curves of Fig. 7(b) show higher values for m at later times. Moreover, Fig. 7(a) referring to a larger distance from the grating compared with Fig. 7(b) indicates a significantly higher value of m from the beginning of field oscillations. This may be explained by the lower contributions of evanescent waves to the light field at a larger distance from the grating.

Next we would like to consider the intensity evolution of the electric field E_x vs time in close proximity to the grating. Figure 8 provides a comparison between the intensities $|E_x|^2$ at (a) $z=h+0.008$ μm and at (b) $z=h+0.300$ μm. Both plots of Figs. 8(a) and 8(b) indicate periodic changes in intensity with a reciprocal increase and decrease at $x=0$ and $x=a_g/2$. The high peak intensity at $x=0$ of Fig. 8(a) is explained with the electromagnetic field enhancement in the immediate vicinity of the grating surface due to the excitation of SPPs.[4,13] In Fig. 8(a) the mean intensity for $x=0$ is larger than for $x=a_g/2$ while the reverse is true for Fig. 8(b).

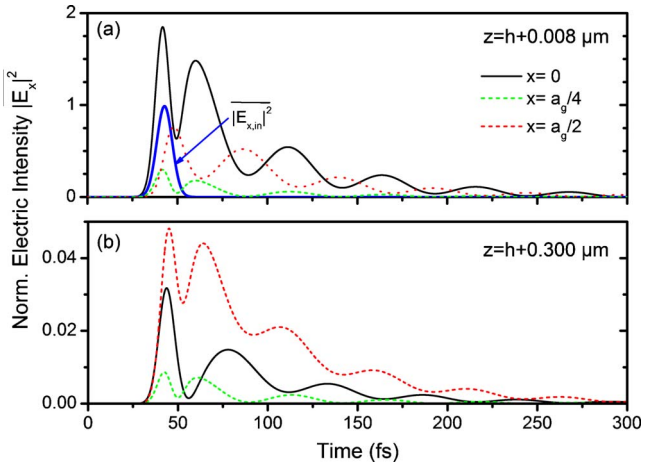

FIG. 8. (Color online) Light intensity $\overline{|E_x|^2}$ related to the peak intensity of the incident pulse vs time, (a) 8 nm and (b) 300 nm above the grating at different transverse locations x. The intensities at $x=a_g/4$ and $x=a_g/2$ of plot (a) have been increased by a factor of 200 and 10, respectively. The blue curve indicates the intensity of the incident Gaussian pulse.

Thus, brightest near-field intensity should be detected in and around a grating slit while much lower intensity is observed between adjacent slits at very close proximity to the grating. However, at 300 nm distance from the grating the situation is different: the strongest light intensity is now between the slits. These results are qualitatively consistent with measurements at continuous-wave excitation.[24]

Figure 9 displays the Poynting flows $\bar{S}_{z,norm}$ and $\bar{S}_{x,norm}$ in the z and x direction, respectively, at distances of (a) 8 nm and (b) 300 nm above the grating. Let us first consider the maximum Poynting flow $\bar{S}_{z,norm}$ (black solid line) of Fig. 9(a), which exhibits periodic changes of the flow direction at a grating aperture. These oscillations correspond to a regular

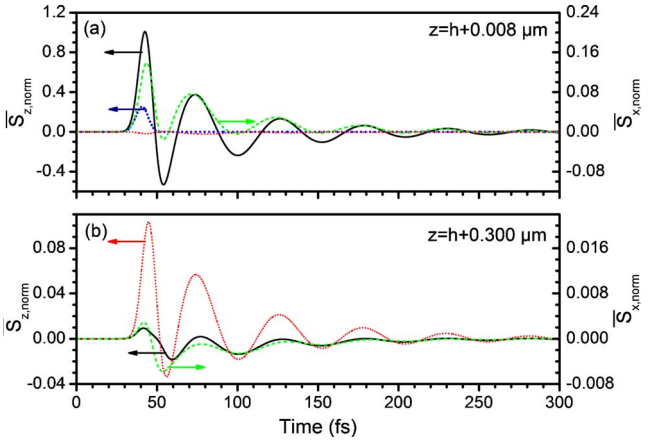

FIG. 9. (Color online) Poynting flows $\bar{S}_{z,norm}$ and $\bar{S}_{x,norm}$ related to the peak value of the incident Poynting flow as functions of time at (a) 8 nm and (b) 300 nm above the grating. The left vertical axes relate to $\bar{S}_{z,norm}$, the right ones to $\bar{S}_{x,norm}$. Solid black lines and dotted red ones correspond to $\bar{S}_{z,norm}$ at $x=0$ and $x=a_g/2$, respectively. Dashed green curves refer to $\bar{S}_{x,norm}$ at $x=a_g/4$.

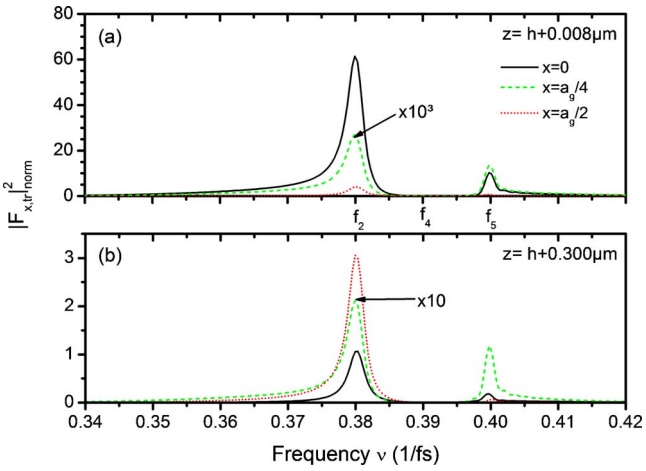

FIG. 10. (Color online) E_x near-field spectra (a) 8 nm and (b) 300 nm above the grating at three different transverse locations x as indicated. The spectral densities $|F_{x,tr}|^2_{norm}$ are related to the peak value of the incident spectral density corresponding to a Gaussian pulse.

exchange of field energy between the SPPs on the top and bottom surfaces through the grating slits. Figure 9(b) indicates that 300 nm above the grating the major part of $\bar{S}_{z,norm}$ (dotted red line) is located just between two adjacent slits, i.e., at $x=a_g/2$. The Poynting flow $\bar{S}_x$ (dashed green line) in x direction relates to the transverse energy transport, which changes its flow direction periodically, in accordance with the normal component $\bar{S}_z$ of the Poynting flow. For comparison, Fig. 9(a) also contains the Poynting flow $\bar{S}_{z,norm}$ assigned to the carrier wavelength $\lambda_0=1.10$ μm, which is represented by the dotted-dashed blue curve. In this case, $\bar{S}_{z,norm}$ shows no change in the flow direction but points toward the positive z axis during the entire period of light transmission. From this, we conclude that the changes in the Poynting flow direction for $\lambda_0=0.79$ μm are due to the influence of the SPPs. This corresponds to the occurrence of frequency beating on the transmitted and reflected electric fields at $\lambda_0=0.79$ μm which is also attributed to the presence of SPPs while no beating is observed at $\lambda_0=1.10$ μm, see Figs. 2(a) and 2(b).

We conclude this chapter with Figs. 10(a) and 10(b), representing the optical spectra (squared moduli of the Fourier transforms vs. frequency) of the E_x near fields (a) 8 nm and (b) 300 nm above the grating. First we see from Fig. 10 that the maxima of both spectra are at the same frequency f_2, however, they significantly differ from each other in their transverse locations, i.e., $x=0$ for (a) and $x=a_g/2$ for (b). For all the cases shown in Figs. 10(a) and 10(b), the peak of $|F_{x,tr}|^2_{norm}$ generally appears at f_2.

At the flat-metal SPP resonance f_4 we observe a minimum transmission for all transverse positions displayed in Fig. 10. The same holds true for the spectra at a distance as far as 3.75 μm above the grating, as shown in Fig. 3(a). A recently published paper reports on experimental and theoretical results of the spectral near- and far-field characteristics of a grating that consists of a thin gold film deposited onto a sapphire substrate.[26] The authors measured a dip at f_4 in the

far-field spectrum, which is consistent with the respective result following from our model. However, they observed a peak at f_4 in the near-field spectrum, in contrast to our finding above. The sapphire substrate is the essential difference between the grating of Ref. 26 and our theoretical grating model. The SPP flat-metal resonance frequencies on the top and bottom interfaces are generally different in a grating deposited on a substrate with a refractive index larger than unity while they agree in case of a free-standing grating surrounded by air, as was assumed in our model. Therefore, the coupling between the SPPs on the two interfaces will be much stronger in the latter case.

We conclude that a different strength of SPP mode coupling on the grating interfaces results in different spectral characteristics of the near and far fields. A more detailed study on spectral properties, especially those of the near field, will be reserved for future investigations.

IV. TIME-RESOLVED SPECTRA

A. Wavelet transform

In chapter III light fields in the vicinity of a grating and optical spectra associated with these fields have been presented. The time-independent spectra were determined from the fields by Fourier transformation, where, as usual, the integration extends over the entire time axis $(-\infty \le t \le +\infty)$. However, to gain a more detailed insight into the plasmon dynamics it would be desirable to understand how the amplitude of spectral components in the light field varies with time.

The wavelet transformation is a well-established method for analyzing a complex temporal and spectral evolution of an electromagnetic field. Its name comes from a short oscillatory function (wavelet) that controls a windowed Fourier transform by scaling and translation parameters, see below. Probably the most widely used wavelet is the Gabor wavelet, which reads as[50]

$$\psi(t) = g(t)e^{i\eta t} \equiv \frac{1}{(\sigma^2\pi)^{1/4}} e^{-t^2/2\sigma^2 + i\eta t}, \tag{7}$$

where $\int_{-\infty}^{+\infty} |\psi|^2 dt = 1$. Equation (7) indicates that the Gabor wavelet behaves like a damped oscillator characterized by finite temporal and spectral widths.

The temporal half width (FWHM) of the Gaussian function $\psi(t)$ on the right-hand side of Eq. (7) is given by $\Delta t_h = 2\sqrt{2\ln 2}\sigma$ while the width of the corresponding Fourier transform $\hat{\psi}(\omega)$ is $\Delta\omega_h = 2\sqrt{2\ln 2}/\sigma$. The Function $\psi(t)$ of Eq. (7) is called the mother wavelet, the prototype for generating daughter wavelets, which read as

$$\psi_{u,s}(t) = \frac{1}{\sqrt{s}} \psi\left(\frac{t-u}{s}\right) \tag{8}$$

with a translation parameter u and a scaling factor s.

The wavelet $\psi_{u,s}(t)$ is centered at delay u and frequency η/s in the time-frequency plane. The temporal and frequency variances attributed to this center point are defined via

$$s^2\sigma_t^2 = \int_{-\infty}^{+\infty} (t-u)^2 |\psi_{u,s}(t)|^2 dt$$

and

$$\sigma_\omega^2/s^2 = 1/2\pi \int_{-\infty}^{+\infty} (\omega - \eta/s)^2 |\hat{\psi}_{u,s}(\omega)|^2 d\omega,$$

where σ_t^2 and σ_ω^2 denote the respective variances with respect to the mother wavelet $(u=0,\ s=1)$. For a Gabor wavelet one obtains $\sigma_t^2 = \sigma^2/2$ and $\sigma_\omega^2 = (2\sigma^2)^{-1}$.

With respect to time and frequency the variances are linked according to Heisenberg's uncertainty principle. In the present case of a Gaussian-shaped Gabor wavelet, the uncertainty relation attains its minimum $\sigma_t^2\sigma_\omega^2 = 1/4$. The time and frequency coordinates cannot be specified to an accuracy better than $s\sigma_t$ and σ_ω/s. Rectangular Heisenberg boxes, centered at $(u, \eta/s)$, of width $s\sigma_t$ in time and σ_ω/s in frequency illustrate the temporal and spectral spread in the time-frequency plane, see below. Useful relations connecting the full half-widths of the Gabor wavelet and its Fourier transform with the standard deviations are $\Delta t_h \approx 3.3\sigma_t$ and $\Delta\omega_h \approx 3.3\sigma_\omega$.

A wavelet transform (WT) of a scalar signal function $f(t)$ is defined as follows:[50]

$$Wf(u,s) = \int_{-\infty}^{+\infty} f(t)\psi_{u,s}^* dt, \tag{9}$$

where $\psi_{u,s}^*$ is the complex conjugate of the wavelet function of Eq. (8). The absolute value of the wavelet transform is called the WT amplitude $A(u,s)$ given by $A(u,s) = |Wf(u,s)|$. In the following we consider characteristic features of two-dimensional functions $A(u,s)$ related to the electric light fields above and below the grating.

To obtain $A(u,s)$ the temporal behavior of $E_x(t)$ numerically calculated in chapter III.B is inserted on the right-hand side of Eq. (9), that is, $f(t) \equiv E_x(t)$. We would like to mention that the squared WT amplitude $A(s,u)^2$ corresponds to $|F(\nu)|^2$ the squared modulus of the Fourier transform defined above. The next chapter shows that time and frequency resolution in the u/s plane is mainly determined by the parameter σ. A small value of σ corresponds to a large half width $\Delta\omega_h$, possibly resulting in a fairly coarse spectral resolution such that frequency intervals of interest are not individually distinguishable. On the other hand, small σ also means high temporal resolution, since Δt_h is small. In fact, the value of σ should be adapted appropriately to get as much comprehensive insight as possible into the spectral evolution with time.

B. Wavelet transforms of light fields in the vicinity of the grating

In what follows wavelet transforms of light field components are presented starting with the WT transform of a beat note as an introductory example (chapter IV.B.1.). In a second step, WT transforms of light fields above and below a grating illuminated with a short pulse are calculated and compared with relevant Fourier spectra (IV.B.2.).

1. Wavelet transform of a beat signal

The light field around the grating fades away over several periods of damped oscillations after the incident pulse dies

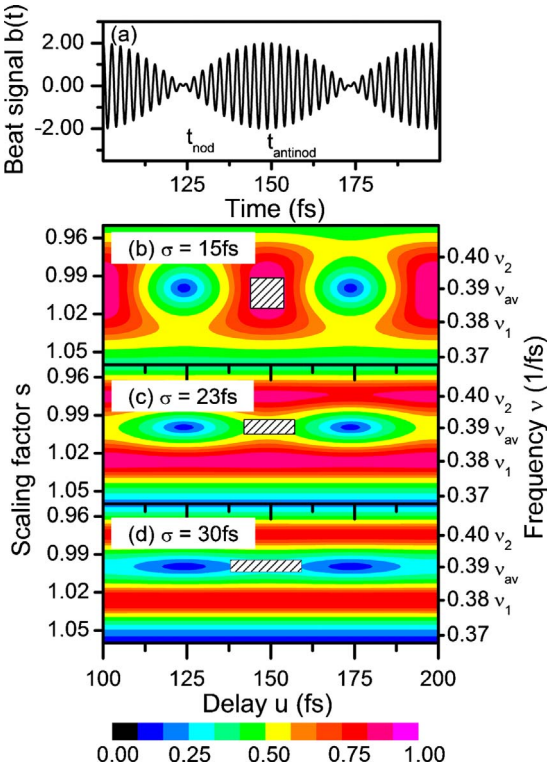

FIG. 11. (Color online) Wavelet transform of a beat signal $b(t)$. (a) Electric field $b(t)$ resulting from two interfering waves of frequencies ν_1 and ν_2. Subsequent plots show the WT amplitude of $b(t)$ for (b) $\sigma=15$ fs, (c) $\sigma=23$ fs, and (d) $\sigma=30$ fs. The ordinates in (b)–(d) relate to scaling factor s (left) and frequency ν (right). The abscissa is the time delay u between wavelet and $b(t)$. Hatched rectangles indicate Heisenberg boxes.

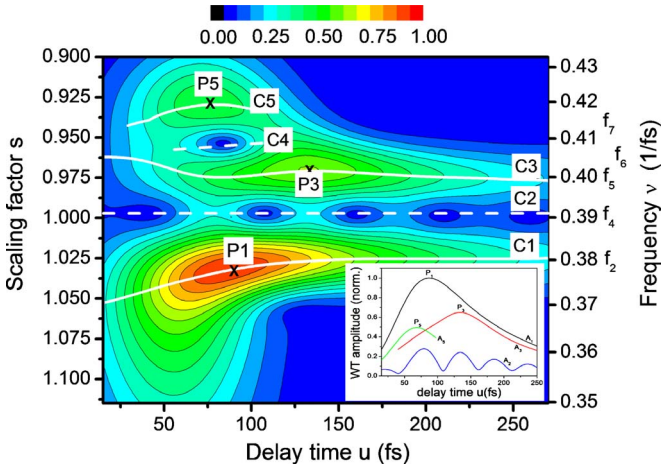

FIG. 12. (Color online) Contour plot of the WT amplitude $A(u,s)$ for the E_x field above the grating, displayed by the red curve in the bottom part of Fig. 2(a). The two-dimensional plot refers to $\sigma=30$ fs. Global maxima of $A(u,s)$ are marked by crosses. White solid lines in the u/s plane join local maxima of $A(u,s)$ while dashed ones connect local minima. Curves A1, A2, A3, and A5 in the inset show WT amplitudes vs u taken along paths C1, C2, C3, and C5, respectively, in the main plot.

out, see Fig. 2. Before presenting wavelet transforms of a calculated light field, we want to give an idea of what a wavelet transform of simple beat oscillations looks like, see also Ref. 51. To this end, we apply a wavelet transformation to two interfering waves $b(t)=\cos(2\pi\nu_1 t)+\cos(2\pi\nu_2 t)$ with $\nu_1=0.38$ fs^{-1} and $\nu_2=0.40$ fs^{-1}. This interference results in a beat frequency $\nu_{beat}=\nu_2-\nu_1=0.02$ fs^{-1}. For a comparison with the beating characteristics of Figs. 2(a) and 2(b), the numerical values of ν_1 and ν_2 were chosen such as to nearly agree with the boundary frequencies of the gap in the Fourier spectrum of Fig. 3(a).

Figure 11(a) shows the beat signal $b(t)$ versus time while the plots of Figs. 11(b)–11(d) indicate the WT amplitude $A(u,s)=|Wf(u,s)|$ following from Eq. (9) with $f(t)\equiv b(t)$ for various values of σ, namely, (b) $\sigma=15$ fs, (c) $\sigma=23$ fs, and (d) $\sigma=30$ fs. The angular frequency η of the Gabor wavelet is chosen as $\eta=2\pi\nu_{av}$, where $\nu_{av}=(\nu_1+\nu_2)/2=0.39/fs$. Moreover, ν_{av} is assumed to correspond to $s=1$. The latter definition leads to the relation $s=\nu_{av}/\nu$, which means that ν_1 and ν_2 are associated with $s=1.026$ and $s=0.975$, respectively. On the right-hand sides of Figs. 11(b)–11(d), frequency axes are additionally introduced to facilitate transformation from scaling factors into frequency and vice versa. Hatched areas of Figs. 11(b)–11(d) indicate Heisenberg boxes belonging to $s=1$. Red-colored areas correspond to high WT amplitudes, blue ones to low amplitudes. We observe a distinct periodic variation of the WT amplitude with delay time for $\sigma=15$ fs, Fig. 11(b), which apparently reflects the intensity variation with time of the beat pattern. The increase in frequency resolution from Figs. 11(b)–11(d) can be explained with a decrease in the spectral halfwidth of the wavelet, $\Delta\nu_h$ relative to $\nu_{beat}=\nu_2-\nu_1$. In detail one obtains $\Delta\nu_h\approx 1.2\nu_{beat}$, $\Delta\nu_h\approx 0.8\nu_{beat}$, and $\Delta\nu_h\approx 0.6\nu_{beat}$ for the plots (b)–(d), respectively. Thus, the frequency resolutions related to (c) and (d) are sufficient to discern separated frequency intervals that contain ν_1 or ν_2.

2. *Wavelet transform of calculated fields above and below the grating*

Returning to the original problem, we proceed with the wavelet transform of the field $E_x(t)$ in the intermediate near-to-far-field region of a grating illuminated by a 10 fs pulse of carrier frequency $\nu_0=0.38/\text{fs}$, see chapter III.B. The transmitted and reflected electric fields appearing in response to the exciting pulse are shown in Figs. 2(a) and 2(b) (red curves). Wavelet transform amplitudes $A(u,s)$ of these fields are shown in Figs. 12 (transmitted field) and 13 (reflected field). The vertical axes correspond to scaling factor (left) and frequency (right), linked together as explained in the previous chapter; the horizontal axis relates to the delay time u.

The two wavelet diagrams, Figs. 12 and 13, relate to $\sigma=30$ fs, allowing for a satisfying frequency resolution $\Delta\nu_h\approx 1.2\times 10^{-2}$ fs^{-1} in the time frequency plane, Fig. 11(d). This value of σ appears also suitable for obtaining insight into the spectral evolution of fields related to more complex wavelet transforms than those in Figs. 12 and 13. We expect, however, only a poor resolution in time according to a halfwidth of $\Delta t_h\approx 70$ fs which is much longer than the incident pulse width but shorter compared to the effective duration of

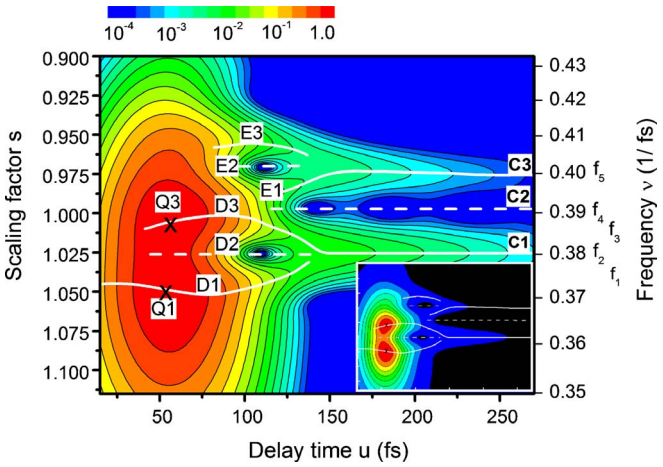

FIG. 13. (Color online) Same as Fig. 12 but for the E_x field below the grating shown by the red curve in the bottom part of Fig. 2(b). Note the logarithmic scale for the WT amplitude $A(u,s)$ in the main plot. White solid lines in the u/s plane join local maxima of $A(u,s)$ while dashed ones connect local minima. The inset reproduces the main plot but employs a linear scale in order to highlight details of the contour relief in the high-amplitude region.

field response. It is easily seen that both plots of Figs. 12 and 13 can be roughly divided into two sections, namely, (i) a main section earlier than $u \approx 120$ fs representing high WT amplitudes and (ii) a subsequent section to the right of $u \approx 120$ fs which shows a much weaker WT amplitude. The low amplitude is evidently related to light emission due to the decay of SPPs, after the disappearance of the initial pulse. We would like to note that the extended time in the main section is due to the previously mentioned large temporal halfwidth of the Gabor wavelet. We further observe a distinct discrepancy in the width of the spectral ranges of the two sections. While the spectral range of the main section is comparable to that of the exciting field, a much narrower spectral width is found in the second section.

The best access to the above WT transforms $A(u,s)$ of Figs. 12 and 13 is probably through a comparison with relevant FT spectra. Let us first focus on Fig. 12 and its FT counterpart, the red curve of Fig. 3(a). The latter FT spectrum exhibits peaks at frequencies f_2, f_5 and f_7 but dips at f_4 and at f_6. These particular frequencies are indicated on the frequency axis of Fig. 12. Curves C1 and C3 represent positions of local maxima in the time-frequency plane while C2 indicates the bottom of a valley between C1 and C3. At large delay times, the frequency coordinates of C1, C2, and C3 are close to f_2, f_4, and f_5, respectively. Thus, the valley of low WT amplitude is associated with the frequency gap of the FT spectrum whereas the curves C1 and C3 correspond to the peaks limiting the frequency gap at its low- and high-frequency sides, respectively, see Fig. 3(a).

Curves C4 and C5 represent traces on the high-frequency wing of the pulse spectrum with frequencies around f_6 and f_7. These curves correlate with the dip at f_6 and the peak at f_7 in the FT power spectrum, respectively. Since they are located outside the SPP frequency gap, the curves C4 and C5 only exist in the presence of the exciting pulse.

The inset of Fig. 12 shows the WT amplitudes along curves C1, C2, C3, and C5 in the main plot. Graph A1 shows a distinct asymmetric behavior resulting from a steep slope of the leading edge and a slow decrease in the trailing edge, which can be explained by a fast decline of the exciting pulse and a comparatively slow decrease of surface plasmon density after the input pulse disappeared. A less pronounced shape is found for curve A3. We further observe that curve A2, the WT amplitude along C2, is damped and periodically modulated which is reminiscent of Fig. 11(d), where similar patterns arise at $\nu = 0.39/\text{fs}$ even though damping was not included.

Figure 13 depicts the WT amplitude of the E_x field reflected from the grating, see red curve of Fig. 2(b). Again, we want to focus on the relationships between characteristic features of WT and FT transforms. Particular frequencies in the FT spectra of Figs. 3(a) and 3(b) are also indicated on the frequency axis of Fig. 13. Let us first look at curves D1 and D3, connecting local maxima in the time-frequency plane. The inset provides evidence that points Q1 and Q3 marked on D1 and D3 indicate positions of global maxima of the WT amplitude. The frequencies attached to Q1 and Q3 agree quite well with f_1 and f_3, respectively, i.e., the frequencies of the two adjacent peaks in Fig. 3(b). Line D2 marks the bottom of a valley between Q1 and Q3, which corresponds to the dip at frequency f_2 of Fig. 3(b).

After delay times related to peaks Q1 and Q3, curves D1 and D3 move away from each other, but eventually change again their direction in the u/ν plane and move toward each other. Ultimately, curves D1 and D2 end at $u \approx 137$ fs whereas D3 continues with line C1 extending to the right edge of the plot. A similar pattern can be observed for a set of curves above frequency f_4 in Fig. 13. In detail, E1 is continued by line C3 which, like C1, extends to the right edge of the plot. On the other hand, curves E2 and E3 also end at $u \approx 137$ fs, just as D1 and D2 do.

It remains to discuss curve C2, which is on the bottom of the valley between lines C1 and C3. Thus, the behavior of curves C1, C2, and C3 at large delay times conforms with that of Fig. 12. This indicates a symmetric SPP decay on the top and bottom interface of the grating long after the exciting pulse has disappeared. We conclude with Fig. 14, which summarizes important features of the wavelet transforms for the grating fields shown above. Figures 14(a) and 14(b) represent cross sections of the WT contour maps of the respective Figs. 12 and 13, parallel to the frequency axis. Each cross section displays the WT amplitude vs. frequency at a particular delay time u. We restrict ourselves to four values of u, namely, $u = 30$, 90, 130, and 210 fs.

First, we note a prominent dip in the WT amplitude close to $f_4 \equiv f_{SP} \approx 0.39$ fs^{-1}, i.e., the frequency of the first-order SPP resonance for a smooth interface. This behavior is visible in all curves of Fig. 14(a), that is, during the total delay-time interval considered. We note further that the wavelet amplitude changes noticeably with u within a narrow frequency interval around f_4. Starting from small values of u, we first observe a large difference in the heights of the two nearest maxima of the WT amplitude on either side of f_4 in the case of $u = 30$ fs and $u = 90$ fs. The height difference of the two maxima levels out, however, again with increasing u as can be seen, for example, in the WT amplitude for $u = 210$ fs. The transient behavior of the peak heights is also

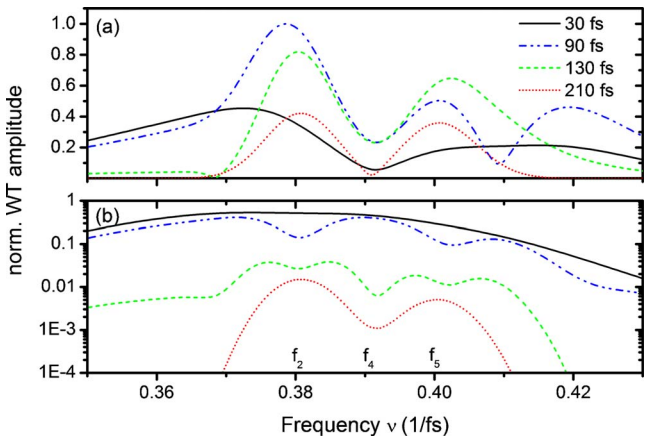

FIG. 14. (Color online) WT amplitudes of the electric field E_x at particular delay times u vs frequency. (a) 3.75 μm above and (b) 3.75 μm below the grating. The curves are taken from Figs. 12 and 13, respectively, and relate to various values of u, namely, black solid lines correspond to $u=30$ fs, blue dotted dashed ones to $u=90$ fs, green dashed curves belong to $u=130$ fs, and red dotted lines to $u=210$ fs. The WT amplitudes of (a) and (b) are normalized to their respective peak values. Note the logarithmic scale for the ordinate of (b).

evident from the graphs A1 and A3 in the inset of Fig. 12. Moreover, Fig. 14(a) indicates a remarkable variation in the dip amplitude with time. While the minimum values of the WT amplitude close to f_4 are very low for $u=30$ and 210 fs, significantly larger minimum values are obtained at $u=90$ fs and $u=130$ fs. The temporal change of the dip minimum is described in detail through curve A2 in the inset of Fig. 12.

Next we focus on the situation below the grating, that is on Fig. 14(b). In contrast to Fig. 14(a), we recognize that the WT amplitude of Fig. 14(b) exhibits a dip at f_4 only during the final stage of light emission, i.e., at large u, well after the exciting pulse disappeared. This is illustrated, for example, by the curves for $u=130$ fs and $u=210$ fs. In conclusion, Fig. 14 indicates that a dip in the wavelet amplitude occurs at frequency f_4, both above and below the grating. The dip below the grating becomes discernible, however, only long after the exciting pulse and, in turn, the field reflected of the bottom surface disappears. This means that the spectral characteristics of SPP decay on the top and bottom interfaces reveal a very similar behavior for large times.

V. SUMMARY

In this work we investigated the temporal and spectral properties of the light field around a free-standing transmission gold grating illuminated with a TM-polarized laser pulse of 10 fs duration at normal incidence. The carrier frequency of the pulse was chosen such as to excite SPP modes on the top and bottom air/metal interfaces. In particular, we studied the temporal behavior of the field, which is closely connected to the SPP decay after the impinging pulse disappeared. Our numerical simulations reveal that the near and far fields consist mainly of evanescent or propagating waves, respectively.

In close proximity to the grating, the evanescent waves are propagating parallel to the grating surfaces and interfere with each other, which results in a periodic transverse amplitude modulation. The near-field amplitude modulation exhibits increasing strength with time due to a drop of the evanescent wave density associated with the SPP decay. In the far-field region, the propagating waves of zeroth diffraction order $(q=0)$ are traveling perpendicularly to the grating surfaces and give rise to a homogeneous transverse profile. These far field waves also show temporal amplitude modulation with a period corresponding to the reciprocal width of a frequency gap in the optical transmission spectrum. A strong coupling between SPP modes on the top and bottom interfaces leads to fixed phase relations between the beat notes of the transmitted and reflected light fields. This coupling is confirmed by the periodic change of the near-field Poynting flow with direction perpendicular to the interfaces.

Finally, we studied the time evolution of the spectra for the transmitted and reflected far-fields with a Gabor wavelet transform. A comparison between the main features of the WT amplitudes and those of the relevant Fourier transform spectra indicates coinciding positions of the peaks and dips at the frequency axes for the transmitted fields. In particular, minimum transmission is observed at the flat-metal SPP resonance. In contrast, the WT amplitude of the reflected light shows a peak at small delay times and a dip at large delay times. On both interfaces the same spectral features of the SPP decay can be observed long after the incident pulse vanished.

The excitation of SPPs with continuous-wave and pulsed lasers has found a large variety of applications in nanooptics, for example, in enhanced light transmission through nanostructured metallic films,[11] integrated photonic devices,[52] and optical nanoantennas.[53] The applications mentioned can benefit from a temporal resolution on the femtosecond scale, when ultrashort laser pulses are used for excitation of the SPPs. However, this requires a detailed understanding of the underlying SPP decay. In this paper we presented different aspects to the dynamics of the SPP decay after excitation with ultrashort laser pulses. The wide availability of laser sources in the considered wavelength range (near infrared) allows for a direct experimental testing of the above findings.

ACKNOWLEDGMENT

The authors are grateful to Günter Steinmeyer for fruitful discussions and thorough proofreading of the manuscript.

[1] J. J. Baumberg, T. A. Keif, Y. Sugawara, S. Cintra, M. E. Abdelsalam, P. N. Bartlett, and A. E. Russell, Nano Lett. **5**, 2262 (2005).
[2] Z.-W. Liu, qi-Huo Wei, and Xiang Zhang, Nano Lett. **5**, 957 (2005).
[3] P. Andrew and W. L. Barnes, Science **306**, 1002 (2004).
[4] H. Raether, *Surface Plasmons*, Springer Tracts in Modern Physics (Springer, Berlin, 1988), Vol. 111.
[5] *Near-Field Optics and Surface Plasmon Polaritons*, Topics in Applied Physics, edited by S. Kawata, Vol. 81 (Springer, Berlin, 2001).
[6] W. L. Barnes, A. Dereux, and T. W. Ebbesen, Nature (London) **424**, 824 (2003).
[7] R. W. Wood, Phys. Rev. **48**, 928 (1935).
[8] J. W. S. Rayleigh, Philos. Mag. **14**, 60 (1907).
[9] U. Fano, J. Opt. Soc. Am. **31**, 213 (1941).
[10] A. Hessel and A. A. Oliner, Appl. Opt. **4**, 1275 (1965).
[11] T. W. Ebbesen, H. J. Lezec, H. F. Ghaemi, T. Thio, and P. A. Wolff, Nature (London) **391**, 667 (1998).
[12] H. F. Ghaemi, T. Thio, D. E. Grupp, T. W. Ebbesen, and H. J. Lezec, Phys. Rev. B **58**, 6779 (1998).
[13] U. Schröter and D. Heitmann, Phys. Rev. B **58**, 15419 (1998).
[14] M. M. Treacy, Appl. Phys. Lett. **75**, 606 (1999).
[15] E. Popov, M. Neviere, S. Enoch, and R. Reinisch, Phys. Rev. B **62**, 16100 (2000).
[16] Y. J. Chen, E. S. Koteles, R. J. Seymour, G. J. Sonek, and J. M. Ballantyne, Solid State Commun. **46**, 95 (1983).
[17] D. Heitmann, N. Kroo, C. Schulz, and Zs. Szentirmay, Phys. Rev. B **35**, 2660 (1987).
[18] S. C. Kitson, W. L. Barnes, and J. R. Sambles, Phys. Rev. B **52**, 11441 (1995).
[19] W. L. Barnes, S. C. Kitson, T. W. Preist, and J. R. Sambles, J. Opt. Soc. Am. A **14**, 1654 (1997).
[20] W. L. Barnes, J. Lightwave Technol. **17**, 2170 (1999).
[21] S. Collin, F. Pardo, R. Teissier, and J.-L. Pelouard, Phys. Rev. B **63**, 033107 (2001).
[22] Z. Sun, Y. S. Jung, and H. K. Kim, Appl. Phys. Lett. **83**, 3021 (2003).
[23] C. Ropers, D. J. Park, G. Stibenz, G. Steinmeyer, J. Kim, D. S. Kim, and C. Lienau, Phys. Rev. Lett. **94**, 113901 (2005).
[24] C. Ropers, D. J. Park, H.-W. Ghim, K.-G. Lee, J. Kim, Q. H. Park, D. S. Kim, and C. Lienau, *Conference Paper (QTuA)*, Quantum Electronics and Laser Science Conference (QELS) (Optical Society of America, Long Beach, California, 2006).
[25] Jin E. Kihm, Y. C. Yoon, D. J. Park, Y. H. Ahn, C. Ropers, C. Lienau, J. Kim, Q. H. Park, and D. S. Kim, Phys. Rev. B **75**, 035414 (2007).
[26] D. J. Park, K. G. Lee, H. W. Kihm, Y. C. Byun, D. S. Kim, C. Ropers, C. Lienau, J. H. Kang, and Q.-Han Park, Appl. Phys. Lett. **93**, 073109 (2008).
[27] A. S. Vengurlekar, A. V. Gopal, and T. Ishihara, *Proceedings of the 15th International Conference*, Pacific Grove, USA, July 30–August 4, 2006 (Springer-Verlag, Heidelberg, 2007), p. 651.
[28] M. Weber and D. L. Mills, Phys. Rev. B **27**, 2698 (1983).
[29] H. Lochbihler, Phys. Rev. B **50**, 4795 (1994).
[30] J. A. Porto, F. J. Garcia-Vidal, and J. B. Pendry, Phys. Rev. Lett. **83**, 2845 (1999).
[31] Ph. Lalanne, J. P. Hugonin, S. Astilean, M. Palamaru, and K. D. Möller, J. Opt. A, Pure Appl. Opt. **2**, 48 (2000).
[32] F. J. García-Vidal and L. Martin-Moreno, Phys. Rev. B **66**, 155412 (2002).
[33] P. N. Stavrinou and L. Solymar, Opt. Commun. **206**, 217 (2002).
[34] Q. Cao and Ph. Lalanne, Phys. Rev. Lett. **88**, 057403 (2002).
[35] J. M. Steele, C. E. Moran, A. Lee, C. M. Aguirre, and N. J. Halas, Phys. Rev. B **68**, 205103 (2003).
[36] R. Müller, V. Malyarchuk, and C. Lienau, Phys. Rev. B **68**, 205415 (2003).
[37] R. Müller, C. Ropers, and C. Lienau, Opt. Express **12**, 5067 (2004).
[38] A. Dechant and A. Y. Elezzabi, Appl. Phys. Lett. **84**, 4678 (2004).
[39] K. G. Lee and Q.-Han Park, Phys. Rev. Lett. **95**, 103902 (2005).
[40] N. W. Ashcroft and N. D. Mermin, *Solid State Physics* (Holt, Rinehart and Winston, New York, 1976).
[41] A. Taflove and S. C. Hagness, *Computational Electrodynamics: The Finite-Difference Time-Domain Method*, 2nd ed. (Artech House, Boston, 2000).
[42] St. A. Cummer, IEEE Trans. Antennas Propag. **45**, 392 (1997).
[43] A. Vial, A.-S. Grimault, D. Macias, D. Barchiesi, and M. L. de la Chapelle, Phys. Rev. B **71**, 085416 (2005).
[44] S. H. Zaidi, M. Yousaf, and S. R. J. Brueck, J. Opt. Soc. **8**, 770 (1991).
[45] I. Pockrand, J. Phys. D **9**, 2423 (1976).
[46] P. B. Johnson and R. W. Christy, Phys. Rev. B **6**, 4370 (1972).
[47] B. E. A. Saleh and M. C. Teich, *Fundamentals of Photonics*, 2nd ed. (Wiley-Interscience, Hoboken, New Jersey, 2007).
[48] C. Genet, M. P. van Exter, and J. P. Woerdman, Opt. Commun. **225**, 331 (2003).
[49] M. Sarrazin, J.-P. Vigneron, and J.-M. Vigoureux, Phys. Rev. B **67**, 085415 (2003).
[50] S. Mallat, *A Wavelet Tour of Signal Processing*, 2nd ed. (Academic Press, San Diego, 2001).
[51] K. Gröchenig, *Foundations of Time-Frequency Analysis* (Birkhäuser, Boston, 2001).
[52] M. Sandtke and L. Kuipers, Nat. Photonics **1**, 573 (2007).
[53] P. Mühlschlegel, H. J. Eisler, O. J. F. Martin, B. Hecht, and D. W. Pohl, Science **308**, 1607 (2005).